IEEE Access
Multidisciplinary | Rapid Review | Open Access Journal

Received 25 June 2024, accepted 8 July 2024, date of publication 15 July 2024, date of current version 25 July 2024.

Digital Object Identifier 10.1109/ACCESS.2024.3427844

RESEARCH ARTICLE

Design and Control of a New Pneumatic Quadruped Soft Robot Based on Honeycomb Structure

MENG HONGJUN, ZHANG SHUPENG, ZHANG WEI, AND REN YUKE
School of Automation and Software, Shanxi University, Taiyuan, Shanxi 030006, China

Corresponding author: Meng Hongjun (menghj@sxu.edu.cn)

This work was supported by the Shanxi Scholarship Council of China under the project "Soft Bionic Quadruped Robot Based on Honeycomb Structure" (Project No.: 2022-006).

ABSTRACT Inspired by the flexible structure of soft organisms, many researchers have developed different new soft robots using various flexible materials. Compared with traditional rigid robots, soft robots have a small mass, a high degree of freedom, good flexibility, and high safety of human-computer interaction. However, research on designing new types of quadruped soft robots is still a big challenge. This paper proposes an innovative design and control methodology for a pneumatic quadruped soft robot, employing a highly deformable hexagonal structure with shape-preserving material characteristics. First of all, the scheme design of the bionic soft quadruped robot. Based on the movement mechanism of quadrupeds, combined with the deformation concept of the honeycomb hexagonal chamber, the leg structure of the robot is designed, and the corresponding pneumatic driver is designed according to the driving mode, which can drive the legs to perform stretching, bending and other movements. Secondly, the mathematical modeling and finite element simulation. The deformation principle of the hexagonal chamber and the elongation of a single leg are modeled by the geometric analysis method, and then the validity of the modeling is verified by the finite element simulation method. Finally, multiple experiments show the performance of the designed quadruped robot including the static characteristics, output force, and workspace on a single leg. Besides, the control logic program was used to carry out the straight line and curve walking experiments of the quadruped robot. Thus the proposed method provides an efficient and effective design strategy for soft quadruped robots.

INDEX TERMS Soft quadruped robot, structural design, finite element simulation, motion control research.

I. INTRODUCTION

Different from traditional rigid robots, most soft robots are created inspired by soft biological structures in nature [1], made of soft and elastic materials, with good deformation and adaptability, the main features are flexible body structure and deformation control, its flexible body structure theoretically has infinite degrees of freedom of movement, which is closer to the movement mode of the simulated organism, can realize complex deformation, and can move and operate freely in narrow, complex or irregular environments [2], [3], the obstacle avoidance performance is stronger, and the adaptability and stability to the environment are enhanced; in addition, due to the flexibility of the software structure itself, the contact force to the environment is smaller during work, and the interaction safety is higher. Therefore, soft robots are usually used in extreme conditions or unknown environments. With the continuous development of soft robot technology, people began to apply soft robots in many fields, including medical treatment [4], rescue, manufacturing and entertainment. For example, in the medical field, soft robots can be applied to endoscopic surgery [4], drug delivery [5] and artificial organs [6], [7], which can reduce surgical trauma and improve treatment effects; in the field of rescue, soft robots can Applied to search and rescue and disaster rescue [8], it can perform tasks in complex environments and

The associate editor coordinating the review of this manuscript and approving it for publication was Aysegul Ucar.

improve efficiency; in the process of exploring search and rescue tasks, a robot with light weight, small footprint, and low contact force is required to perform; When fetching tasks, robots with high compliance and adaptability to the shape of the object to be grasped [9], [10] are required to perform, etc.; in addition, soft robots can be applied to movie special effects and robot entertainment, etc., bringing people more nice experience.

As a classic robot form, quadruped robot has good stability and maneuverability, and can adapt to various terrains [1]. Using the high flexibility and deformability of soft materials to apply them to the structural design of quadruped robots can not only better simulate the movement of quadruped organisms, but also improve the adaptability of robots in irregular environments. and stability.

Soft quadruped robots can be used in many fields such as military affairs, agriculture, and rescue, and have broad application prospects. In the military field, soft quadruped robots can be used to perform dangerous tasks, such as complex terrain reconnaissance, bomb disposal, etc.; in the rescue field, soft quadruped robots can be used for disaster rescue, search and rescue [11], etc. Therefore, the research on soft quadruped robots can not only bring new opportunities for the development of robot-related fields, but also promote the improvement of production efficiency and improve the quality of human life. Thus, the research and development of new soft quadruped robot has been a widely expanding subject.

The Biomimetic Robotics Laboratory of Harvard University has been committed to the research of soft robots. They have developed a series of soft robots, the representative ones are Octobot [12] and so on. Octobot is a soft robot driven by inkjet. It is inspired by octopus. It consists of a soft octagonal body and eight soft arms. It is driven by the reaction of hydrogen peroxide and catalyst and can move freely in water. In addition, the Whitesides [13] team, also from Harvard University, designed a soft quadruped robot using a pneumatic network driver, which realizes cable-free drive and can perform large-scale deformation through an area smaller than itself.

Researchers such as Ishida et al. [14] of the University of California developed an underwater quadruped robot with soft legs and soft inflatable deformable body structure. Each leg mechanism is composed of three bellows, and their shapes can be changed by applying pressure changes, thereby affecting the fluid dynamics. Multiple solenoid valves are used to control the inflation and exhaust of each bellow at a velocity of 15 mm/s in static water.

The Octopus [15] developed by the Italian Institute of Biorobotics is an underwater robot consisting of a rigid torso and 8 soft arms, imitating the tentacles of an octopus, capable of moving and grabbing objects like an octopus.

The Self-Defense Robotics Laboratory of the Massachusetts Institute of Technology has developed an earthworm-like soft robot [16]. The robot is driven by a memory alloy, and the outer body is made of polymer materials, which can realize functions such as crawling and rolling. In addition, researchers at Ohio State University have also developed a soft mechanical finger based on the drive method of memory alloy [17], which can achieve large deformation bending and grasping objects. Researchers at Seoul National University have developed a mechanical glove [18], which is driven by a cable, wrapped in silicone on the outside, and the cable is driven by a motor to realize the movement of each finger.

The climbing robot [19] developed by researchers at Worcester Polytechnic Institute can imitate the climbing movement of the inchworm and move on two-dimensional and three-dimensional surfaces. The bionic jellyfish robot designed by researchers such as Najem et al. [20] is driven by an ion-exchange polymer to conduct discharge, so as to control the flexible movement of the robot underwater.

The Eulalie Coevoet team at the University of Lille, France [21] was inspired by the elephant trunk and designed a floppy drive robot driven by cables. There are four cables embedded in it to control the tip of the torso and the deformation trajectory, which can grasp and Turn the object.

Inspired by the flexibility of elephant trunks, Chen Xiaoping's team at the University of Science and Technology of China developed a honeycomb pneumatic network structure [22] soft manipulator, which is driven by multi-layer airbags inside, and the movement of the manipulator is realized by inflating and deflating, which can easily complete multiple operating tasks, such as opening doors, opening drawers, twisting bottle caps, etc., even if there is human interference in the process, the task can be completed accurately. In addition, researchers from Zhejiang University have developed a worm robot using highly elastic materials [23], which imitates the crawling mode of worms, and its degree of deformation can achieve end-to-end connection.

David Danelia et al. set up a test bench to analyze the dynamic characteristics of 3D-printed soft continuum actuators and select the optimal configuration. Next, they constructed a soft quadruped robot, analyzed its standing and walking performance, reduced its weight through a redesign of the electromechanical structure, and conducted gait analysis to achieve walking. Finally, they calculated the transportation cost and compared the efficiency of different gaits [24]. Jiang et al. proposed a pneumatically driven quadruped robot using soft-rigid hybrid rotary joints. Based on the unique rotary joint design, they used joint-level PID controllers to control the angular displacement of the hip and knee joints. They studied typical gait patterns, including walking and trotting gaits, and built and tested a proof-of-concept prototype [25].

The remainder of this paper is organized as follows. The next section describes the overall structure of the designed quadruped robot. This is followed by mathematical modeling based on geometric analysis. Subsequently, the finite element simulation analysis of the single-leg model is

presented. Following this, the experimental research section is discussed, which covers the construction of the control system, performance tests of soft mechanical legs, and gait examples of the designed robot. Finally, the summary of the paper is presented.

The main features of this paper are:

1. Designed and optimized the leg structure of a bionic soft quadruped robot based on a hexagonal honeycomb cavity structure, achieving multiple deformation functions.

2. Verified the mathematical model of a single leg through finite element analysis, ensuring the effectiveness of the design.

3. Developed a multi-channel air pressure control system, successfully tested the performance of the soft mechanical legs and the walking ability of the quadruped robot, and verified its stability and mobility.

II. STRUCTURAL DESIGN AND OPTIMIZATION OF QUADRUPED ROBOT

The goal of the bionic soft quadruped robot designed in this paper is to realize the movement on the plane, mainly including straight walking and curved walking. In order to achieve the above objectives, the soft quadruped robot is required to have the ability of single leg bending, stepping motion and overall turning motion. A large number of studies have shown that the hexagonal structure has a high deformation rate, and its deformation is only a change in the shape of the structure, and the material itself does not expand or change in length [26]. Therefore, we utilize hexagonal structures to innovatively implement a new mechanical leg chamber network. Structure and pneumatic grid driver, analysis, manufacture, assembly, combined with appropriate configuration, developed a bionic soft quadruped robot.

A. STRUCTURAL DESIGN OF SOFT QUADRUPED ROBOT

1) STRUCTURAL DESIGN AND SIMULATION OF SOFT MECHANICAL OUTRIGGERS

Inspired by the hexagonal network structure, we designed a hexagonal chamber grid structure to imitate the single-leg stepping and bending of quadrupeds, as shown in Figure 1(a). Each leg consists of two columns It consists of a hexagonal chamber grid structure, each column includes 16 layers of chamber structure, with a height of H and a width of M, and a connection structure is provided above the outriggers for fixed connection with the body.

The structure of a single hexagonal chamber is shown in Figure 1(b). Among them, we design the six sides to have the same wall thickness as d_1, and the distance between the upper and lower inner surfaces is h_1. In addition, there is a slot at the junction of every two sides, w_1 is the groove depth. In order to allow a single chamber to deform to the greatest extent under a certain safe air pressure without damaging the chamber structure itself, we conduct a finite element analysis of the simulated force in the chamber, and set the initial height $h_1 = 5$ mm during the analysis. Change the two coefficients

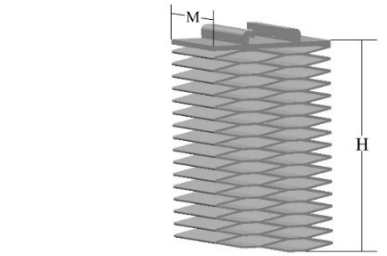

(a) Hexagonal network structure

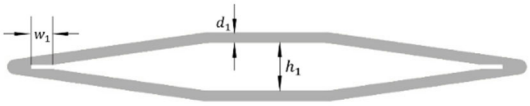

(b) single chamber structure

FIGURE 1. Hexagonal chamber network structure.

d_1 and w_1 to make the height change Δh_1 meet the design requirements. First set $w_1 = 0$ mm, and use the control variable method to analyze the wall thickness d_1. Figure 2(a) shows the deformation effect of a single chamber under a pressure of 50 kPa, and Figure 2(b) shows the relationship between wall thickness d_1 and shape Plot of the variable Δh_1. Among them, the chamber material setting parameters are the same.

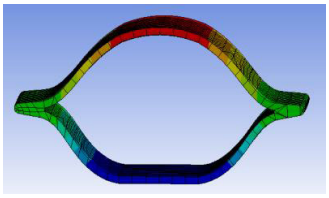

(a) Single-chamber deformation simulation effect

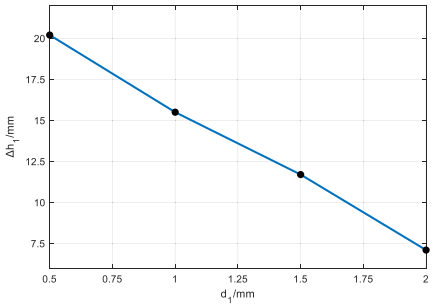

(b) The relationship between chamber wall thickness and deformation height

FIGURE 2. Wall thickness and deformation of single chamber.

Combining the deformation effect in Figure 2(a) and the relationship curve between wall thickness d_1 and deformation Δh_1 in Figure 2(b), we can see that the relationship between d_1 and Δh_1 is approximately linear, the larger d_1 is, the smaller Δh_1 is. However, if the wall thickness d_1 is too small, although a larger deformation amount can be obtained, the structure is prone to instability when the force is applied; and when t he wall thickness d_1 is too large, although the material strength is improved, the deformation amount Δh_1 is small. Therefore, we consider the stability while ensuring the deformation, and determine the wall thickness $d_1 = 1$ mm.

Afterwards, in order to further increase the deformation Δh_1, we carried out the same force analysis as above, and obtained the relationship curve between the groove depth w_1 and the deformation Δh_1. Figure 3(a) shows the deformation effect of a single chamber at a pressure of 50 kPa when $d_1 = 1$ mm; Figure 3(b) shows the relationship between the groove depth w_1 and the deformation Δh_1.

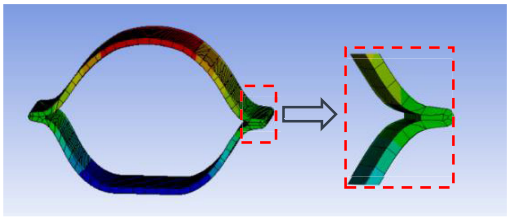

(a) Grooving Depth Deformation Effect

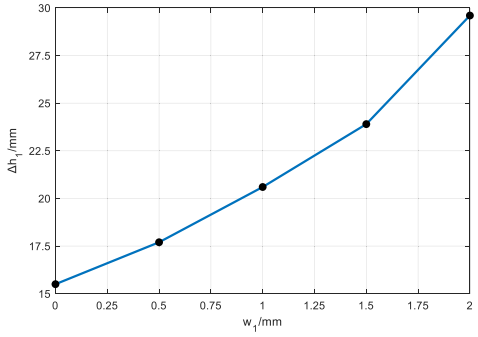

(b) Relationship between slotting depth and deformation

FIGURE 3. Relationship between groove depth and deformation.

As shown in Figure 3(a) and (b), when the wall thickness d1 is constant, increasing the groove depth w1 will further increase the deformation Δh1 of the single chamber, but if w1 is too large, it will easily cause fracture at the junction of the left and right two ends. According to the curve relationship, we choose w1 = 1.5 mm. So far, the parameter optimization design of the single chamber has been completed. After adjustment, the overall design height of the outrigger H0 = 130 mm, and the thickness of the upper connecting platform is 3 mm.

In order to meet the flexibility requirements of imitating the legs of quadrupeds, we divided the soft outrigger into two parts, the large and small femurs, as shown in Figure 4(a), each leg segment contains 8 layers of hexagonal chamber structure. In addition, according to the leg structure and deformation requirements, the legs are further divided into 8 regions, as show in Figure 4(b).

2) GAS DRIVER DESIGN

The pneumatic grid driver is mainly used to drive and deform embedded in the cavity of the soft outrigger, resulting in the corresponding deformation of the leg. In Figure 2-4(b), each leg is divided into 8 areas, and since the actuator used is pneumatic, each actuator needs an air hole. In order to reduce the number of air holes, a folding embedding method is adopted, and one driver is embedded in each area. To this end, we designed a rectangular strip-shaped driver, which is

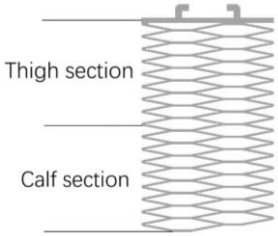

(a) Front view

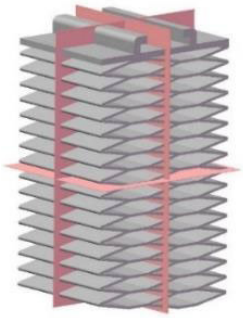

(b) Regional division

FIGURE 4. Schematic diagram of soft robotic legs and regions.

composed of two layers of film, and the interior is divided into 16 grids, corresponding to the 8-layer chamber structure on each leg segment. In other words, two layers of aerodynamic grids are embedded in each chamber. Driver structure is shown in Figure 5.

Figure 5(a) illustrates the structure of the pneumatic grid driver, where each grid is approximately square. Inside the driver, 16 air ducts are arranged to ensure communication between grids. In the process of embedding the pneumatic driver into the legs of a soft quadruped robot, there are two different shapes of air pathways: yellow pathways effectively connect adjacent chambers, while using only blue pathways may lead to airflow obstruction. Stomata connect to the electric proportional valve, facilitating inflation and deflation. The green arrows indicate the process of gas inflating the pneumatic driver from the electric proportional valve through the Stomata, while the red arrows indicate the deflation process. Among the 16 air ducts inside the driver, 8 short ducts are used for gas circulation between two layers of grids within the same chamber, and 8 long ducts are used for gas circulation between adjacent chambers.

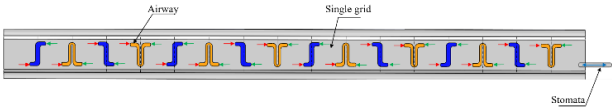

(a) Pneumatic drive structure

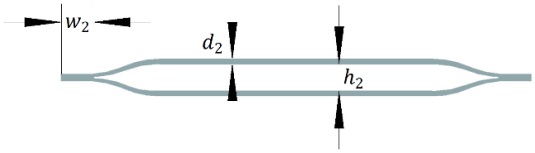

(b) Pneumatic Driver Single Mesh Side View

FIGURE 5. Pneumatic drive structure.

Figure 5(b) shows the side view of the single grid of the driver, where w_2 is the edge width on both sides of the driver, d_2 is the thickness of the film, and h_2 is the height of the single grid inside the driver. When the actuator grid is supplied with a certain air pressure, the air pressure acts on each internal wall surface, making h_2 gradually increase, and the inside of the grid is deformed, so that the entire actuator forms an outward expansion force, and returns to the original state after deflation. The d_2 and w_2 remain unchanged throughout the inflation and deflation process.

The pneumatic grid actuator needs to be handcrafted. Before formal production, we purchased PE films of various thicknesses to conduct ultimate burst tests to determine the maximum pressure range that a single grid of the actuator can withstand, thereby determining the parameters for the sealing width w_2 and film thickness d_2. First, we set a larger sealing width value to ensure that the grid edges do not rupture or leak under higher pressures, and then we tested the film thickness d_2. The experimental results, as shown in Figure 6, indicate that the film thickness d_2 has a linear relationship with the ultimate pressure P. However, when d_2 is too large, the film becomes difficult to fold and seal. For safety and work fatigue considerations, and under the condition that the pressure P does not exceed 100 kPa, we selected a thickness of $d_2 = 0.24$ mm. The sealing width test results showed that the ultimate pressures for sealing widths of 2 mm, 3 mm, and 5 mm are 50 kPa, 80 kPa, and 150 kPa, respectively. After comprehensive consideration, we chose a sealing width of $w_2 = 5$ mm.

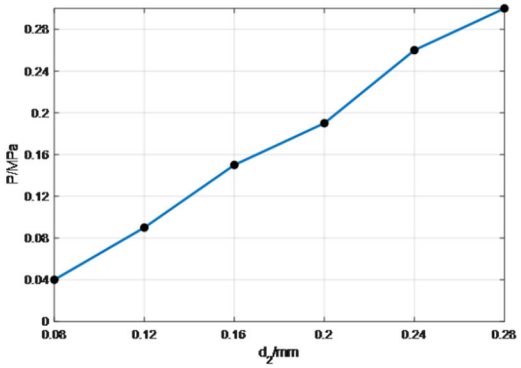

FIGURE 6. Relationship between film thickness and pressure limit.

As shown in Figure 7, the process is divided into 14 steps. First, the entire PE film needs to be divided into several sections at 3.5 cm intervals, and then cut with a hand knife. Next, use a laminator to seal both sides of the cut PE film strips to half their length, as shown in steps 4 and 5 of Figure 1. Then, place the cut air ducts from step 3 In the fixed positions on the upper half of the PE film strips in order of length, maintaining each individual chamber at 2.5 cm, and use the laminator to secure them, as shown by the yellow lines in step 13. The subsequent steps follow steps 4-13, ensuring that the upper half of the PE film strips have 7-8 chambers and the entire PE film strip has 17 chambers.

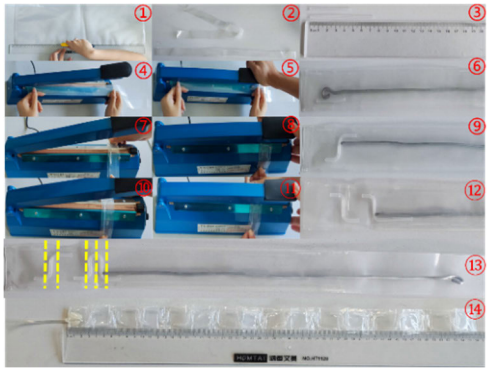

FIGURE 7. Fabrication process of pneumatic grid actuator.

After determining the parameters w2 and d2 for the pneumatic grid actuator, use a laminator to cut the PE film into long strips and seal the short and long edges. The air duct has an inner diameter of 1.5 mm and an outer diameter of 2.5 mm. Arrange the ducts inside and seal them with the laminator to form 16 square grids. After completing the installation of the air ducts, connect the other end of the actuator to a thicker air tube to serve as the air pressure supply port, and seal it with hot melt glue. The size parameters are shown in Table 1.

TABLE 1. Drive size parameters.

Length (mm)	Width (mm)	Edge Sealing Width d_2 (mm)	FilmThickness w_2 (mm)	Grid Side Length (mm)
60	35	5	0.24	25

3) STRUCTURAL DEFORMATION OF SOFT MECHANICAL LEGS

In order for the soft quadruped robot proposed in this paper to be able to walk in a straight line, curve and some basic movements, the soft outriggers must be able to step and lift the legs independently, and the outriggers are required to be able to achieve different degrees of elongation and multi-directional movement. Actions such as bending and 'S' shape. We divide the mechanical outrigger into two parts, the large and small leg segments, that is, each leg segment contains an 8-layer hexagonal cavity structure. Combined with the designed pneumatic grid driver, 8 pneumatic grid drivers are respectively embedded in 8 areas of the soft mechanical leg according to the design requirements, as shown in Figure 8. By filling different air pressures into different actuators, the soft outriggers can be deformed accordingly, that is, the action effect of the outriggers. Figure 9(a) shows the side bending effect of the outrigger, Figure 9(b) shows the forward and backward bending of the outrigger, and Figure 9(c) shows the 'S' shape when imitating walking. In addition, at the bottom of the outriggers, two long strips of soft pads are installed using silica gel to increase the friction between the legs and the ground and prevent the

quadruped robot from sliding while walking. The cushion is simple in structure and light in weight, and its weight is negligible relative to the entire outrigger, and will not bring excessive burden to the movement of the outrigger.

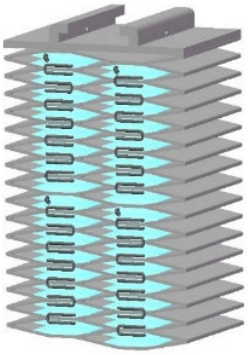

FIGURE 8. The overall structure of the leg.

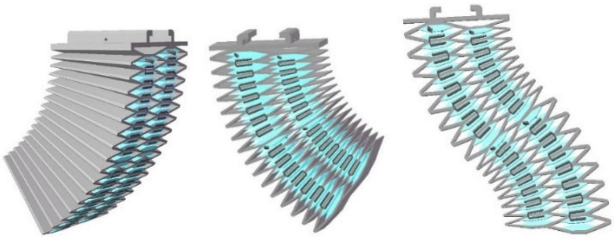

FIGURE 9. Soft mechanical leg and deformation diagram.

B. THE OVERALL STRUCTURE OF THE QUADRUPED ROBOT

The design of the body part of the robot includes a base (divided into front and rear parts), a torsion structure and a horizontal holding structure, as shown in Figure 10. Among them, the twisting structure of the waist is used to turn the body, so as to realize curved walking. Its structure is similar to that of soft outriggers, consisting of two columns of 8-layer hexagonal chamber structures, with two pneumatic grid drivers embedded inside. Left and right rotation can be realized by filling one-sided air pressure. The two ends of the torsion structure are respectively connected to the front and rear base parts, and are fixed with screws to prevent falling off. Since the torsion structure is made of soft materials, in order to prevent the waist from collapsing, a horizontal holding device is fixedly installed directly below it, so as to ensure that when the waist rotates, the bases at both ends are always kept on the same level, and the front and rear bases are strengthened. Seat connection strength. The left and right ends of the base are designed as steps, which are respectively used to connect the software outriggers. In addition, the end face is also provided with a row of holes, which can be further inserted into the screw to fix the legs. At the same time, the distance between the legs at both ends can be flexibly adjusted to facilitate the adjustment of the overall center of gravity of the robot.

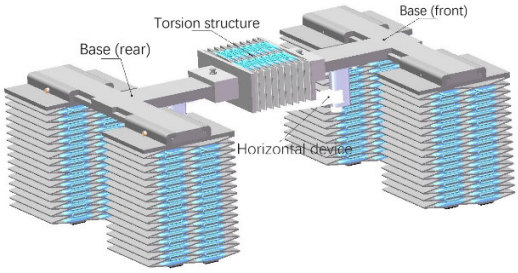

FIGURE 10. Overall body structure design of the robot.

C. PREPARATION OF QUADRUPED ROBOT

The quadruped robot's various parts have different structural requirements, necessitating the selection of multiple materials. The mechanical leg frame and the waist twisting structure both feature a hexagonal chamber structure. When subjected to high pressure, the chamber shape can change, but the material does not stretch. Therefore, a non-stretchable polyurethane elastomer (TPU) with high flexibility is chosen. This material is highly tough, wear-resistant, has good processing performance, and strong chemical resistance, making it suitable for soft structure fabrication. The pneumatic grid driver consists of two layers of film and multiple air ducts, requiring high-temperature sealing and the ability to fold when embedded into the leg frame. Polyethylene (PE) with high flexibility is chosen for this purpose, as it has low tensile strength, good impact resistance, and can withstand high pressure, meeting the driving needs. The front and rear bases and the horizontal stabilizing structure serve as the central connection of the robot, requiring the connection of four mechanical legs. The material needs to be high in hardness but not overly heavy, so T-rulers from the laboratory are used for processing. Screws and bolts needed for connections are replaced with ordinary metal screws. The specific parameters of the selected materials are shown in Table 2.

TABLE 2. Materials and parameters.

	Density (g/cm^3)	Hardness (A°)	Young 's modulus (MPa)	Poisson 's ratio	Color
TPU	1.2	70	80	0.38	Orange
PE	0.95	50	500	0.41	translucent

The structure of the quadruped robot designed in this article includes the external frame of the soft mechanical legs, the waist twisting structure, and the horizontal stabilizing structure, all of which are produced using the A6 3D printer from Shenzhen Aurora. After drawing the models in Solidworks and converting them to .stl files, they are imported into the slicing software JGcreat for setting the printing parameters. Due to the numerous structural components and the need for a moderate printing speed, the entire printing process takes about a week. The printing parameter settings for various materials are shown in Table 3.

TABLE 3. Material and printing parameters.

	Wall Thickness (mm)	Infill Density (%)	Nozzle Temperature	Wall Thickness (mm)	Infill Density (%)
TPU	1.2	60	210	55	65
PLA	1.1	70	220	55	70

III. MATHEMATICAL MODELING OF QUADRUPED ROBOT

Because the driver in each hexagonal chamber in the soft mechanical leg expands and deforms after being filled with certain air pressure, the deformation of each chamber increases. At first, the upper and lower surfaces of the pneumatic grid driver are in almost full contact with the inner surface of the chamber, but as the air pressure increases, the degree of deformation increases, the driver becomes elliptical, and the contact area between the driver and the four sides on both sides gradually decreases. The object becomes the upper and lower surfaces, as shown in Figure 11, which is a schematic diagram of the deformation of a single chamber.

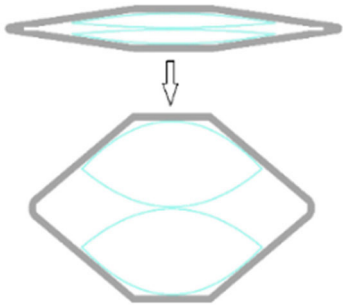

FIGURE 11. Chamber deformation process.

Through the analysis of the deformation process of the chamber in Figure 11, it can be seen that the effect of the driver makes the deformation of the chamber larger. Due to the increase of the upper and lower heights of the chamber and the compression towards the middle, the angle between the left and right sides of the chamber also increases, and the angle can reach 180° under ideal conditions. But in reality, the greater the deformation, the greater the pressure of the air pressure, and the harder the surface of the actuator film becomes, which limits the closeness of the left and right ends of the chamber. At the same time, due to the stretching of the material, the upper and lower heights are also limited within a certain range. In addition, there are force limits and safety air pressure principles inside the driver, and the air pressure should not be too large. In addition, there is a limit to the deformation of the outer leg frame. Therefore, when the actual deformation reaches a maximum value, the angle between the left and right sides of the chamber may be less than 180°.

Different from the traditional rigid quadruped robot, although the kinematics of the soft mechanical outrigger designed in this paper is similar to that of traditional robots, each leg segment will be accompanied by a change in length when it is stretched or bent. In addition, soft-bodied mechanical legs have theoretically infinite degrees of freedom, which makes kinematic modeling more difficult. In order to solve this problem, this paper uses the geometric analysis method to carry out static modeling analysis on a single outrigger, combined with dividing each leg into two parts, the large and small femur, and the four drivers in each part are the same. Based on this situation, the following assumptions are made:

1. Each leg segment can be abstracted into a uniform arc with equal curvature when driven to bend;

2. The deformations of the big and small femurs are independent of each other, that is, the current attitude change of a certain femur is only related to the driving amount of the driver of this femur.

Wherein, ignoring the structural difference on both sides of the outrigger frame, in the initial state (zero air pressure), the lengths of the two rows of chambers remain the same, and the deformation of the two rows of chambers is also the same after being filled with the same air pressure. Figure 12 below shows a side view of a quadruped robot with one leg bent. There are two rows of drivers distributed in its vertical direction, and each row is divided into two leg sections, which can be filled with different air pressure combinations, so the bending directions of each leg section are independent of each other. For example, the air pressure in the left column is greater than the air pressure in the right, and the legs bend to the right. At this time, a bending angle is formed between the two top planes.

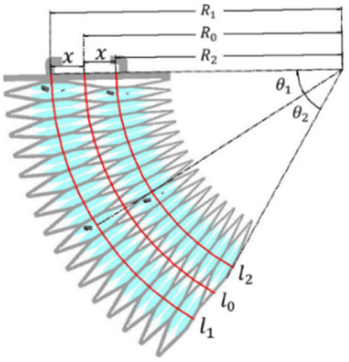

FIGURE 12. Side view of a single leg bent.

As shown in Figure 12 above, we define the bending angles of the thigh and femur as θ_1 and θ_2, and the bending directions of the two are independent of each other; the bending arc length of the high-pressure side is l_1, and the bending radius is R_1; the bending arc length of the low-voltage side is l_2, The bending radius is R_2; in order to facilitate the establishment of the subsequent coordinate system, the length of the bending arc defining the central axis of the leg is l_0, the bending radius is R_0, and the distance from l_1 and l_2 is x.

Taking the single thigh segment as an example, the relationship between the three arc lengths and the bending angle can be expressed as:

$$\frac{1}{2}l_0 = \frac{\pi}{180^\circ}\theta_1 R_0 \tag{1}$$

$$\frac{1}{2}l_1 = \frac{\pi}{180^\circ}\theta_1 R_1 \tag{2}$$

$$\frac{1}{2}l_2 = \frac{\pi}{180^\circ}\theta_1 R_2 \tag{3}$$

$$R_1 - R_2 = 2x \tag{4}$$

$$R_1 + R_2 = 2R_0 \tag{5}$$

Simultaneous formulas (2)∼(4), there are:

$$\theta_1 = \frac{180^\circ(l_1 - l_2)}{4\pi x} \tag{6}$$

Among them, the value of x will change with the change of air pressure, which needs to be analyzed separately. Due to the different air pressures filled in the chambers on both sides, the deformation amount is different, and the change of the chamber height is also different, so there are the following two situations:

1. The deformation of the chamber on the high pressure side is larger than that on the relatively low pressure side;

2. Even if one side of the chamber is filled with air pressure and the other side is at zero air pressure, the height of the chamber on the zero air pressure side will change to a certain extent due to the force anisotropy of the structure.

According to the above situation, a part of the two rows of hexagonal chambers was cut and analyzed. Figure 13 is a simplified schematic diagram of some chambers, where the value of x is calculated as follows:

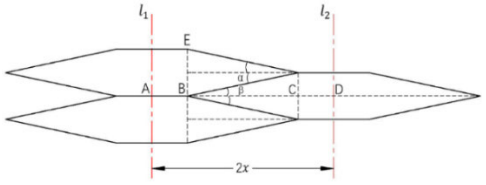

FIGURE 13. Static analysis of chambers on both sides.

According to the analysis in Figure 13, it can be seen that during the deformation process of the chambers on both sides, the height BE changes, and the angles α and β change accordingly, that is, the length of BC is a variable. Assuming that the left chamber is on the high-pressure side, its deformation is greater than that of the right chamber, and the four α angles in the two chambers on the left increase, and the β angle in the right chamber will increase accordingly due to its stretching force. large, while the right angle in the right chamber is not affected. Therefore, in the case of ignoring the material force error, it can be considered that $\alpha = \beta$, and the following relationship can be obtained:

$$\begin{aligned} BC &= BF \cdot \cos\beta \\ &= BF \cdot \sqrt{1 - \sin^2\beta} \\ &= BF \cdot \sqrt{1 - \sin^2\alpha} \\ &= BF \cdot \sqrt{1 - \left(\frac{BE}{2BF}\right)^2} \end{aligned} \tag{7}$$

$$x = \frac{1}{2}(AB + BC + CD) \tag{8}$$

Among them, since the lengths of the six sides of the chamber are equal and fixed for the design, that is, $AB = CD = 7.5$ mm, $BF = EF = 15$ mm; at the same time, l_1 and l_2 are the deformation heights on both sides of the mechanical leg, including the thickness of the platform (3 mm) and the wall thickness of the 17-layer chamber (1×17 mm), so:

$$BE = \frac{l_1 - (3 + 17)}{16} = \frac{l_1 - 20}{16} \tag{9}$$

Simultaneous Eq. (7), (8), (9) get:

$$\begin{aligned} x &= \frac{1}{2}\left(AB + BF \cdot \sqrt{1 - \left(\frac{BE}{2BF}\right)^2} + CD\right) \\ &= \frac{1}{2}\left(15 + 15\sqrt{1 - \left(\frac{l_1 - 20}{480}\right)^2}\right) \\ &= \frac{1}{2} \cdot 15\left(1 + \sqrt{1 - \left(\frac{l_1 - 20}{480}\right)^2}\right) \end{aligned} \tag{10}$$

It can be seen from Eq. (10) that the value of x is only related to the deformation l_1, and when l_1 increases, the value of x will decrease. Combine it with Eq. (5) to get:

$$\theta_1 = \frac{180^\circ\,(l_1 - l_2)}{\pi \cdot 30\left(1 + \sqrt{1 - \left(\frac{l_1 - 20}{480}\right)^2}\right)} \tag{11}$$

Substituting Eq. (11) into Eq. (1)∼ Eq. (3), we get:

$$R_1 = \frac{180^\circ l_1}{2\pi \cdot \theta_1} = \frac{15 \cdot l_1\left(1 + \sqrt{1 - \left(\frac{l_1 - 20}{480}\right)^2}\right)}{l_1 - l_2} \tag{12}$$

$$R_2 = \frac{180^\circ l_2}{2\pi \cdot \theta_1} = \frac{15 \cdot l_2\left(1 + \sqrt{1 - \left(\frac{l_1 - 20}{480}\right)^2}\right)}{l_1 - l_2} \tag{13}$$

Substituting Eq. (12) and Eq. (13) into Eq. (5), we get:

$$R_0 = \frac{R_1 + R_2}{2} = \frac{15\,(l_1 + l_2)\left(1 + \sqrt{1 - \left(\frac{l_1 - 20}{480}\right)^2}\right)}{2\,(l_1 - l_2)} \tag{14}$$

So far, the relational expressions of θ_1 and R_0 about the deformation on both sides have been obtained respectively. Next, the spatial coordinates are used to simplify the analysis. As shown in Figure 14, the black arc is l_0. Three Cartesian spatial coordinate systems $\{O_1\}$, $\{O_2\}$, $\{O_3\}$, the positive direction of the X-axis is the red direction, the positive direction of the Y-axis is the green direction, the positive direction of the Z-axis is the outward direction of the vertical view, the rotation axis is the Z-axis, and the positive direction of the rotation is counte1rclockwise, The straight-line distances between adjacent coordinates are

a_1 and a_2 respectively; the bending radii of the big and small femurs are R_0, $R_0\prime$ respectively, and the height and stride of each leg are: H_1, H_2, S_1, S_2 respectively.

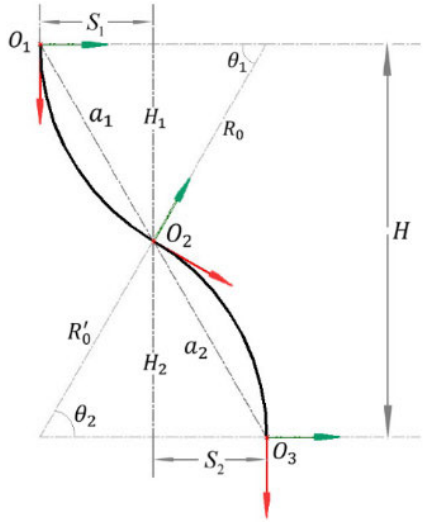

FIGURE 14. Simplified diagram of the single-leg 'S' model.

From Eq. (11), (14)

$$\theta_2 = \frac{180^\circ\,(l_2 - l_1)}{\pi \cdot 30\left(1 + \sqrt{1 - \left(\frac{l_2 - 20}{480}\right)^2}\right)} \tag{15}$$

$$R_0' = \frac{15\,(l_1 + l_2)\left(1 + \sqrt{1 - \left(\frac{l_2 - 20}{480}\right)^2}\right)}{2\,(l_2 - l_1)} \tag{16}$$

From Figure 14, the following relationship can be drawn:

$$a_1 = 2R_0 \sin\frac{\theta_1}{2} \tag{17}$$

$$a_2 = 2R_0' \sin\frac{\theta_2}{2} \tag{18}$$

$$H_1 = R_0 \sin\theta_1 \tag{19}$$

$$H_2 = R_0' \sin\theta_2 \tag{20}$$

$$S_1 = R_0(1 - \cos\theta_1) \tag{21}$$

$$S_2 = R_0'(1 - \cos\theta_2) \tag{22}$$

Through the above relationship, we get the static model of a single leg. Among them, the bending angle and bending radius of each leg segment of a single leg are calculated through the deformation of the chamber, so that the straight-line distance between the two ends of each leg segment during deformation can be calculated, which provides a basis for the subsequent kinematics construction. Models provide a theoretical basis.

IV. FINITE ELEMENT SIMULATION ANALYSIS OF SINGLE-LEG MODEL

A. SINGLE-LEG EXTENSION SIMULATION

In the air pressure-bending angle mathematical model established, it can be seen that the bending angle is related to the arc length (elongation) on both sides, and the air pressure value determines the elongation. In order to verify the correctness of the model, the finite element method was used to simulate the elongation and bending angle of the soft outrigger, and the corresponding variable values under different air pressure values were obtained.

The whole finite element simulation is divided into 7 steps. First, use Solidworks software to model and simplify the three-dimensional model of the soft mechanical leg, and save it as a Step file that can be imported into the finite element software Ansys; the second step: set the material parameters in Ansys; the third step: convert the model Step format file import and configure materials separately; Step 4: Mesh division; Step 5: Add fixed load and adjust pressure value; Step 6: Perform analysis settings and enable large deformation; Step 7: Perform analysis and wait for simulation After success, the displacement and deformation information of the leg after being subjected to pressure can be intuitively obtained through the visualization module.

According to the simulation results of the elongation, as shown in Figure 15, the analysis shows that the elongation also increases with the increase of air pressure. Another obvious phenomenon is that the end of the legs will be inclined to a certain extent, and as the air pressure increases, the angle of inclination will also increase. The reason for this phenomenon is that the bottom structures of the chambers on both sides of the legs are different, with a difference of about half the height of the chambers, which results in amplified structural differences during large deformations. However, when the peak elongation is reached, the corresponding inclination angle is only 6°, so it can be considered that the influence on the follow-up research work is small. The curve relationship is drawn according to the simulation data, as shown in Figure 16, it can be known that with the increase of air pressure, the elongation gradually increases, but the growth rate gradually slows down. When the air pressure is greater than 30 kPa, this phenomenon is more significant.

B. SINGLE-LEG FLEXION SIMULATION

The relationship between air pressure and elongation is obtained through simulation. Since the deformation of the chamber is basically the same under the same air pressure, the overall elongation of the leg can be used as the bending arc length of the inflated side under the corresponding air pressure. In addition, to verify the correctness of the mathematical model of the bending angle and bending radius when the unilateral leg is inflated, we also need to perform a leg bending simulation. As with the elongation simulation process, it is necessary to apply pressure on one side of the chamber and gradually increase the pressure. As the pressure increases, the amount of bending deformation of the leg will gradually increase. The simulation results are shown in Figure 17.

Since the bending angle of the two ends cannot be obtained directly, we need to draw extension lines for the two ends in the resulting image, find their intersection, and measure the

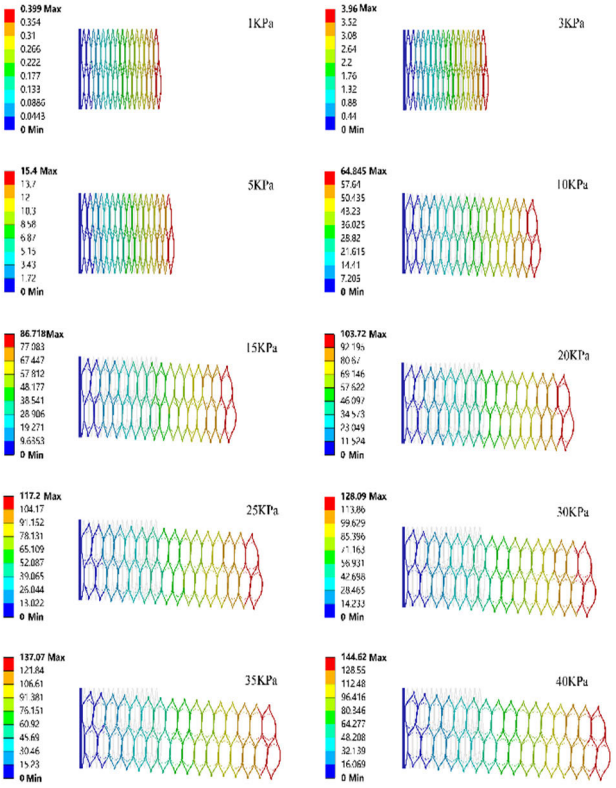

FIGURE 15. The finite element simulation results of elongation.

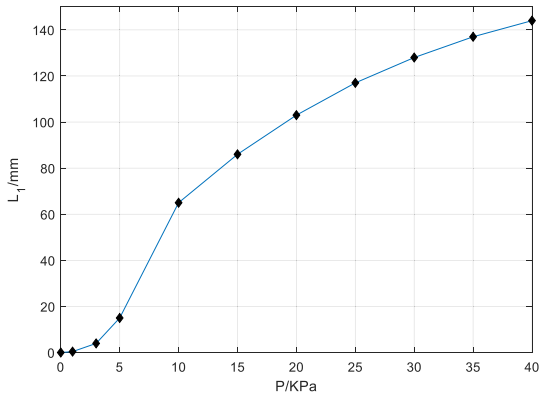

FIGURE 16. Air pressure and elongation simulation curve.

corresponding bending angle and bending radius. In addition, due to the anisotropy of the structural force, the height of the chamber on the non-pressure side (that is, its bending arc length) will also change to a certain extent. We calculated its deformation according to the simulation result data and the static model. We used MATLAB to draw the relationship curve of the bending angle and bending radius data of the chambers on both sides, as shown in Figure 18. It can be seen that the greater the air pressure, the greater the bending angle, and the corresponding bending radius gradually decreases. The deformation of the chamber on the non-pressure side also increases, and the changing trend of the two gradually slows down. Figure 18(d) shows the comparison between the simulation and the static theoretical model. It can be seen

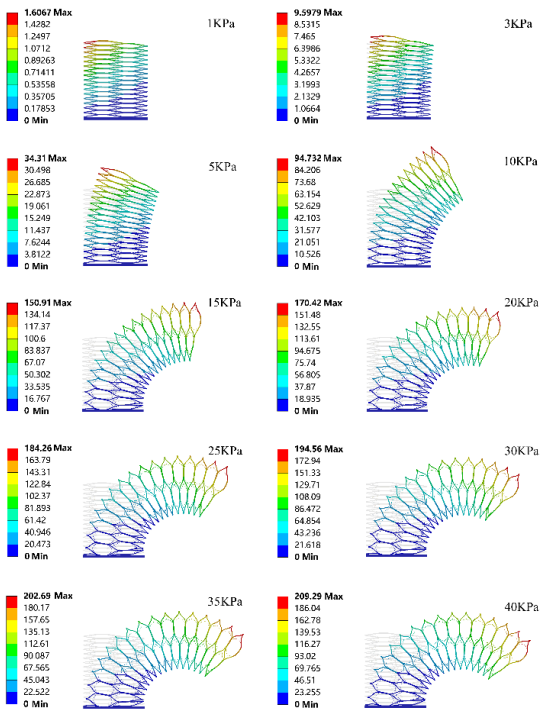

FIGURE 17. Simulation results of air pressure and bending angle and radius.

from the changes in the two curves that the error between the two is small, and the calculated maximum error does not exceed 13%. Similar to the curve of the theoretical model, the relationship between the elongation and bending angle of the simulation results is almost linear, which indicates that the corresponding relationship between air pressure, elongation and bending angle in the simulation process can be applied to the static theoretical model.

V. EXPERIMENTAL RESEARCH ON QUADRUPED SOFT ROBOT

A. THE OVERALL SCHEME OF THE CONTROL SYSTEM

In order to control the work of each driver in the soft quadruped robot more effectively and conveniently, a pneumatic control system for the quadruped robot is designed in this paper. The specific schematic diagram of the control system is shown in Figure 19. The pneumatic control system mainly includes an air compressor (air pump), constant voltage conversion power supply, upper computer PC, data acquisition card, NI myRIO platform, electric proportional valve, etc.

The air pump is produced by Aotusi Industrial and Trade Co., Ltd., model OTS-1100, with a rated exhaust pressure of 0.7 MPa, a gas flow rate of 100 L/min, and a rated power of 1100 W, which well meets the needs of experimental research. The pressure-reducing valve is an accessory of the air pump, with a working range of 0-600 kPa (0-6 bar). It is simple and convenient to use, capable of accurately adjusting the air pressure to 0.1 MPa and maintaining stable output.

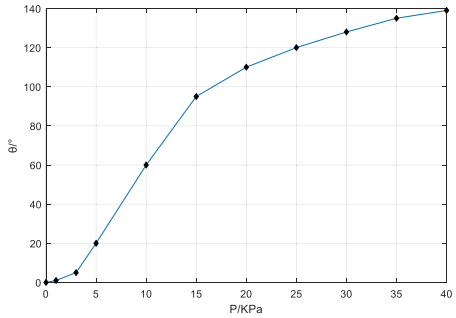

(a) The relationship between pressure and bending angle

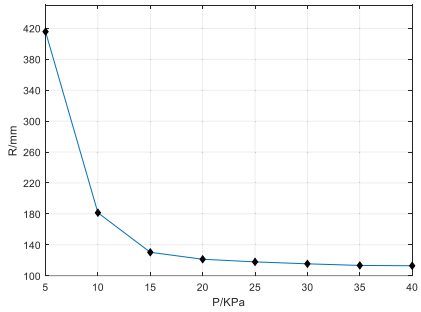

(b) The relationship between pressure and bending radius

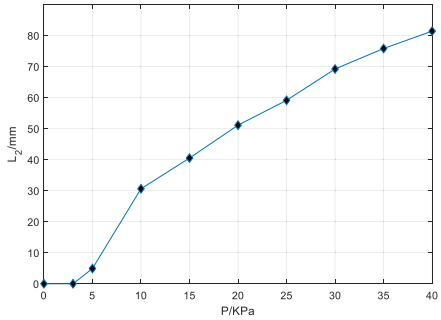

(c) Bending arc length change on the non-pressure side

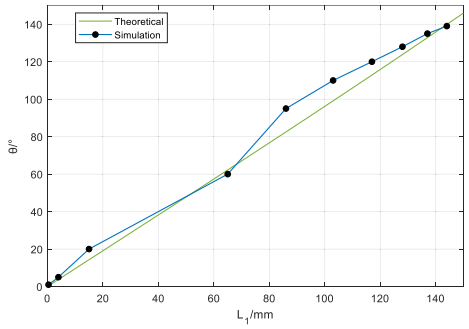

(d) Comparison of simulation results with theoretical models

FIGURE 18. **Simulation result data curve.**

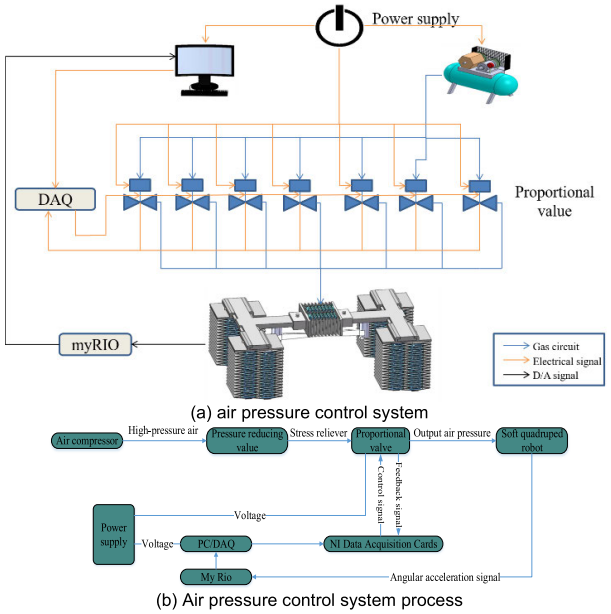

FIGURE 19. **Air pressure control system.**

TABLE 4. **ITV0030-3BS specifications.**

Performance	Parameters
Pressure Range	0.001-0.5 MPa
Maximum Supply Pressure	1.0 MPa
Maximum Flow Rate	6L/min(ANR)(Supply Pressure: 0.6 MPa)
Power Supply Voltage	DC 24 V±10%，DC 12-15 V
Input Signal	DC 0-5 V，DC 0-10 V
Analog Output Signal	DC 1-5 V,Output Accuracy: Within ±6%

The working principle of the electric valve is to achieve stepless control of air pressure (i.e., compressed air) through an electrical proportional signal. The Japanese SMC monolithic ITV0030-3BS thin-type electric proportional valve is chosen. The specific specifications of the electric valve are shown in Table 4.

Each electric valve requires the simulation of air pressure signal input and output. The Advantech PCI-1724U data acquisition card is selected, which features 32 isolated analog output channels, each equipped with a 14-bit DAC. The output range is flexible and can be set through software.

In the entire pneumatic control system, there are two kinds of transmission signals including gas and control signals. According to the signal transmission form, the control system can be divided into the following two parts:

1. Air circuit: The air compressor (air pump) is the air pressure supply source, which is connected to the pressure-reducing valve by a special pipeline. The pressure-reducing valve is used to set the maximum air pressure range required to adjust the output; The air pipes are respectively connected to the input ports of 18 electric proportional valves, and then output to each driver through the output ports of the electric valves (including 32 drivers inside the 4 legs and 2 drivers inside the twisting structure of the waist of the body). The air pressure output of the electric proportional valve is determined by the software and the control module;

2. Control signal part: including electrical signals and digital signals, including hardware devices such as constant

voltage conversion power supply, data acquisition card, upper computer PC, NI myRIO, and software control modules such as DAQ driver and Labview program. First, the control logic program is written by the upper computer Labview software and DAQ driver, and the digital signal is sent out, and the corresponding voltage signal value (corresponding to the input air pressure signal of the electric valve in equal proportion) is output to the terminal adapter board through the data acquisition board in the host computer, and then the signal is transmitted to the control signal terminal of the electric proportional valve through the input signal line, thereby adjusting the opening of the electric valve to adjust the pressure of the air circuit, so that the electric valve outputs the corresponding proportional air pressure to the driver inside the robot in real-time. The control system is used to manage the air pressure of multiple air circuits, so as to adjust the gas with different air pressures to enter the soft actuator, so as to realize various movements of the quadruped soft robot. By controlling the air pressure, the soft actuator can drive the bending or elongation of the external structure to complete different actions.

While the air pressure in the driver rises, the electric valve will be adjusted to the set value, and the real-time voltage signal feedback will be transmitted to the data acquisition card through the monitoring signal line, and real-time display and monitoring can be performed through the program interface. In addition, the deflection angular acceleration signal of the robot will also be fed back through the signal collected by NI myRIO and displayed in real-time on the control program interface

Figure 19 shows the flow of the air pressure control system, in which the constant voltage power supply provides the working voltage for the electric proportional valve, the data acquisition card is responsible for the acquisition and output of the air pressure signal, the host computer PC outputs and processes the signal output from the data acquisition card, through the Labview program Perform logical processing, and then control the air pressure output by the electric proportional valve, thereby controlling the air pressure input into each airbag structure, the duration of inflation and deflation, and the time interval, so that each soft mechanical leg can be deformed or bent to a certain extent, and control The cooperation of the gait movement between the four mechanical legs realizes the straight forward or backward movement of the quadruped robot. If the quadruped robot walks in a curve, in order to bend the body, the body twisting device needs to be rotated to a certain desired angle, and NI myRio is used to feed back the angular acceleration information during the movement process, thereby realizing the curved walk of the quadruped robot.

B. PERFORMANCE TEST OF SOFT MECHANICAL LEGS

The aerodynamic quadruped soft robot proposed in this paper, its core part is the leg and waist torsion parts composed of a hexagonal chamber grid frame structure and multiple pneumatic drives inside it. These structures are the premise and guarantee for the flexible movement of the soft quadruped robot in this paper, and the high flexibility of its movement is also the key to the bionic quadruped. In addition, the output force provided by the driver enables the robot legs to overcome the force of gravity to take steps and realize walking and other motions on the horizontal plane. Therefore, it is necessary to study the performance of single-leg exercises. As mentioned above, a single leg can realize the whole or single-leg segment elongation and bending deformation movement.Therefore, this experiment measures the relationship between the elongation of a single leg and the air pressure, as well as the relationship between the bending angle and the air pressure, and uses it as the driver and indicator of leg motion performance.

1) ELONGATION PROPERTY TEST

In this experiment, the relationship between air pressure and vertical elongation was tested on four soft mechanical legs, that is, the elongation of a single leg was measured by charging different air pressure values. In order to reduce the accidental error in the measurement process and consider the fatigue of the material, it is necessary to conduct 5 experiments on each leg to obtain the average value, and then obtain the average value for the 4 legs. In addition, considering overcoming the factor of self-gravity, during the experiment, put the leg upside down and fix it on the test bench to make it stretch vertically upwards, as shown in Figure 20(a) is the effect diagram of the single leg stretching experiment. After experimental measurement, the elongation of the single leg joint of the leg is half of the overall elongation, which is in line with the design principle, so the overall elongation experiment is used for calculation instead. In order to intuitively express the relationship between the vertical elongation L of the single leg and the air pressure P obtained in the experiment, the final measured data of the experiment were drawn into a graph in MATLAB. Figure 20(b) is a comparison of the relationship between air pressure and elongation under the two conditions of experiment and simulation.

It can be seen from Figure 20(b) that as the air pressure increases, the output pressure of the driver increases, which increases the deformation and elongation of the legs. Since the output pressure of the driver causes the external chamber structure to expand and deform, it is necessary to exceed the minimum deformation air pressure (the minimum deformation air pressure refers to the air pressure required by the hexagonal chamber structure for initial deformation) to generate strain. In the air pressure stage of 0-3 kPa, the legs do not elongate and deform. In this stage, a large amount of energy absorbed by the air pressure is used to overcome the internal force of the structural material to do work, that is, the minimum deformation air pressure is 3 kPa, and it is verified by comparison with the finite element simulation results. In the stage of 3-30 kPa, the bending angle gradually increases with the increase of air pressure,

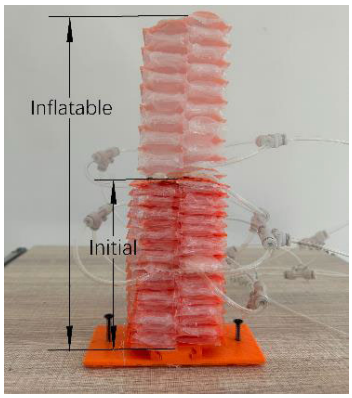

(a) elongation deformation

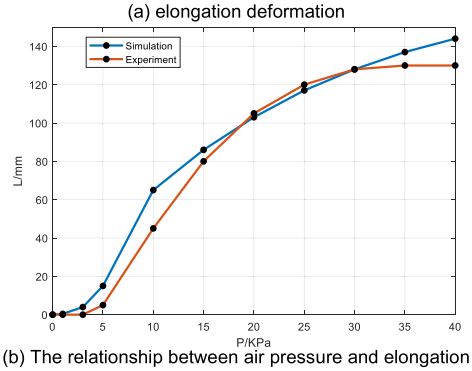

(b) The relationship between air pressure and elongation

FIGURE 20. Elongation experimen.

but its growth rate gradually slows down, and reaches the maximum deformation when the air pressure is 35 kPa. Since the simulation process does not take into account the maximum deformation limit of the actuator strength and the chamber material, as well as the size limit of the actuator, after exceeding 35 kPa, the error with the experimental results is relatively large. The calculated error between the experimental and simulation results is not more than 15%, especially in the 15-30 kPa stage, the error is less than 5%. Within the allowable range of error, the experimental and simulation results are basically consistent.

2) BENDING CHARACTERISTIC EXPERIMENT

In this experiment, the single leg was first placed upside down and fixed, mainly by filling air pressure into the driver in a row of chambers on one side to make it bend to the left or right, and after it stopped changing or stabilized, measure the planes at both ends The angle formed between them, the experimental process is shown in Figure 21. Since the measurement method is manual measurement, in order to reduce errors, the method of taking the average value of multiple measurements is adopted as in the elongation characteristic experiment, and the left and right bending angles and radii of the four legs are measured respectively, and then the data are processed and calculated.

Based on the above-mentioned test platform and method, the air pressure range of one side is controlled by the electric proportional valve to be 0-40 kPa, and the pressure

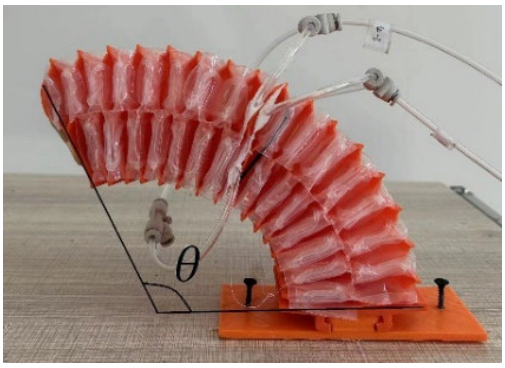

FIGURE 21. Bending experiment.

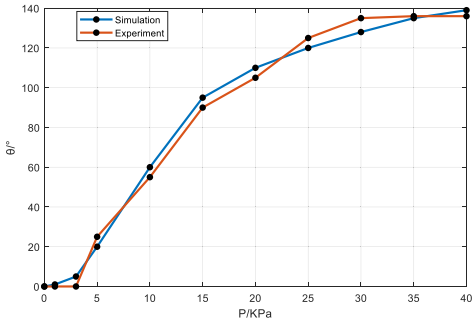

(a) The relationship between air pressure and bending angle

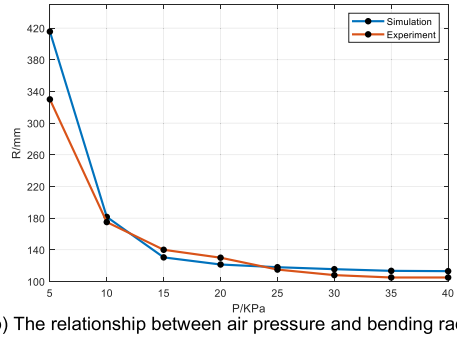

(b) The relationship between air pressure and bending radius

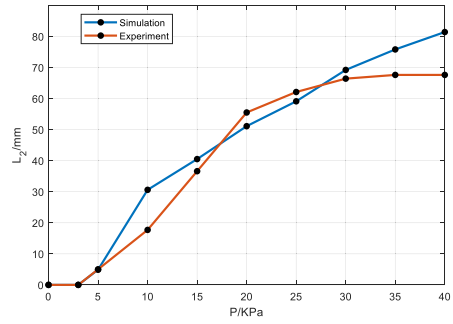

(c) Arc length deformation of the non-pressure side

FIGURE 22. Relationship between air pressure and bending amount.

gradient is 5 kPa, and the corresponding bending angle and bending radius are measured respectively. The experimental results are shown in Figure 22. As shown in Figure 22(a) and (b), with the increase of air pressure on one side, the bending angle gradually increases, that is, the angle formed by the two ends of the legs gradually increases, while the bending radius gradually decreases, and the rate of change of the two gradually slows down until reaching

the deformation limit at 35 kPa and cannot continue to bend. Similar to the experimental results of the above-mentioned relationship between air pressure and elongation, due to the minimum deformation air pressure, the leg structure does not undergo bending deformation in the stage of 0-3 kPa. In addition, in the process of bending, another phenomenon can be observed. Due to the structural tension caused by the deformation of the high-pressure side, the chamber on the other side filled with no air pressure will also undergo a certain amount of expansion deformation and will not maintain the original shape. The length, which is a normal situation, can be calculated in combination with the modeling relationship in Chapter 3, and its deformation is shown in Figure 22(c).

According to the single-leg static model and finite element simulation, combined with the experimental results, the corresponding relationship between the elongation and the bending angle in the three cases is drawn, as shown in Figure 23. The errors of the three mainly come from the fact that the soft mechanical legs have obvious characteristics of the minimum air pressure when starting deformation. Specifically, the deformation of the actuator is not obvious in the low air pressure stage, and it has obvious inertia in the initial deformation stage, so it needs to consume a certain amount of energy generated by air pressure;When the air pressure reaches the critical air pressure (this air pressure is the minimum air pressure to start the deformation), there will be a sudden change in the elongation and bending angle. This phenomenon is more obvious in the experiment. When the air pressure is greater than the critical air pressure, the curves of the three are within a certain air pressure stage. There is a linear growth trend, which is a major cause of error at low air pressure; another reason for the error is that the static model of leg bending and the finite element simulation model is based on the assumption of a uniform arc of equal curvature, but the actual experiment process is not absolute. Uniform arcs of equal curvature. In summary, combined with the finite element simulation and experimental results, the validity of the single-leg static model is verified within the error range.

3) FOOT WORKSPACE EXPERIMENT

In order to achieve effective walking, the single leg is required to undergo an "S" shape deformation, and the air pressure relationship corresponding to the stride S and height H when the single leg is walking needs to be measured, that is, the working space of the foot end when the single leg is walking is measured. The trajectory of its movement is recorded by the camera. Since the single leg is divided into 8 areas, two rows of drivers in each area are combined to inflate and deflate at the same time. In order to carry out this experiment, the drivers in the inner diagonal area of each leg can be further combined, that is, the combination of 1 and 3 areas, and the combination of 2 and 4 areas. When charging the air pressure in the experiment, you can first fill in areas 1 and 3 to make the legs deform in an 'S' shape to the right for

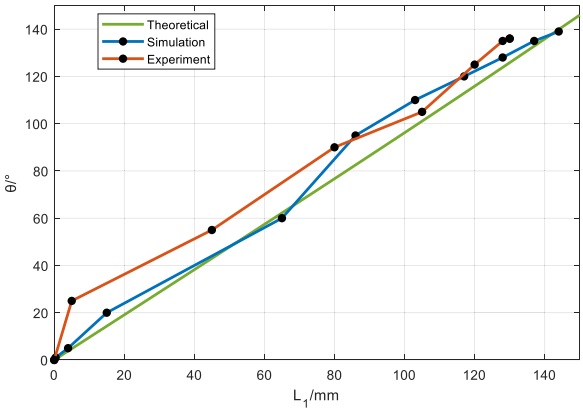

FIGURE 23. Theoretical, finite element simulation and experimental curves.

stepping action, and then fill in areas 2 and 4 to change the height of the feet and adjust the vertical height of the single leg. In addition, considering the influence of gravity and simulating the striding movement to the greatest extent, when measuring the height, the fixed direction of the leg is shown in Figure 4-13, with the end facing upward; when measuring the stride, the fixing method is opposite to the former, which is the leg end down. Figure 24 is the effect of an 'S' type movement of one leg to the right.

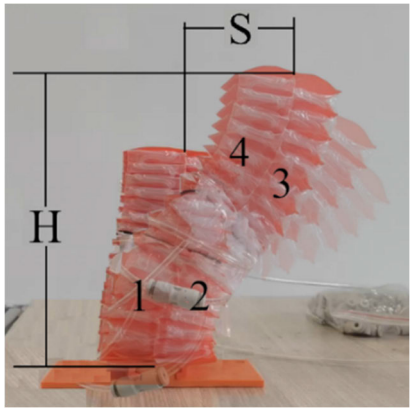

FIGURE 24. 'S' shaped deformation of a single leg.

After the experiment is completed, the measured relationship data between the inflated air pressure in the two diagonal areas and the deformation height H of the foot and the stride S are processed and fitted by MATLAB, and a three-dimensional surface is drawn, as shown in Figure 25 (a, b). It can be seen that as the air pressure in areas 1 and 3 increases, the stride S gradually increases, while the height H shows a trend of first increasing and then decreasing. This is because when the deformation begins, area 1 expands and deforms, resulting in the With the further increase of the air pressure, when the right bending angle of area 1 increases to the maximum, if the air pressure continues to increase, the bending radius will decrease, and H starts to decrease at this time. When the area of diagonals 2 and 4 starts to inflate, the obvious phenomenon is that the height H increases, but the

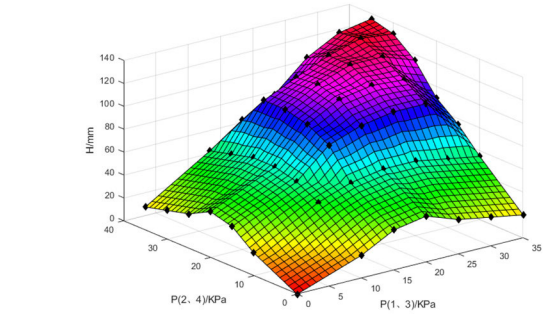

(a) The relationship between air pressure and height H in the diagonal area

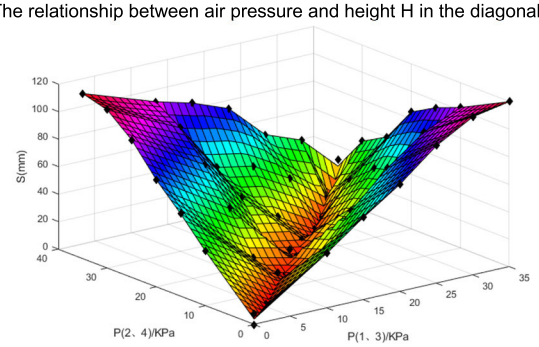

(b) The relationship between the air pressure in the diagonal area and the stride S

FIGURE 25. The relationship between air pressure and deformation in the diagonal area of a single leg.

step size S decreases. When the air pressure in the four areas is equal, the height is the same as the experimental data of the elongation characteristics, but due to the different structure of the bottom of the chambers on both sides, even in the elongated state, the end will be inclined to a certain extent, which is the same as that in Section 3.3.1 The results of the finite element simulation are consistent.

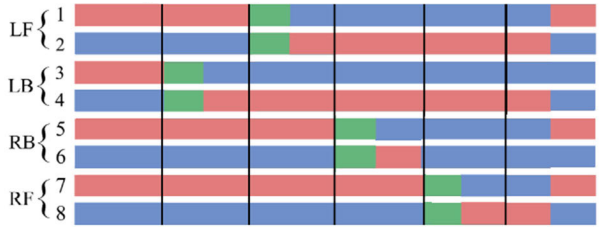

FIGURE 26. Sequence diagram of straight line air path.

C. GAIT EXPERIMENT OF QUADRUPED ROBOT

1) STRAIGHT LINE TEST

A soft quadruped robot needs 16 pneumatic actuators inside the four legs to achieve straight walking. If an electric proportional valve is used to control one actuator, a total of 16 electric valves are required. In order to reduce the number of electric valves and improve the ventilation efficiency, the single-leg driver combination step method in the 4.3.4 experiment was adopted when walking, that is, the combination of 1 and 3 regions, and the combination of 2 and 4 regions. This method can double the number of control air circuits, requiring a total of 8 electrical proportional valves. In order to reduce the impact force when the feet of each leg land on the ground, we design the feet to be as parallel to the horizontal ground as possible when landing. It can be considered that the bending curvatures of the large and small leg joints are approximately equal, that is, the diagonal areas of the two leg joints are filled with air pressure the size is the same, but the order of the high-voltage side and the low-pressure side is reversed. After filling the air pressure into areas 1 and 3, the outriggers do forward S steps, and then fill in lower air pressure in 2 and 4 to make the feet fall slowly and support them parallel to the ground. Write the Labview gait program according to the Walk gait timing plan, control the driver to inflate and deflate, and make the four legs of the quadruped robot move in sequence to realize walking. Figure 26 is a time sequence diagram of the control air circuit.

Among them, red indicates that the diagonal area is in a state of high pressure, blue indicates that the diagonal area is in a state of low pressure, and green indicates that the corresponding area is in the process of deflation. The electric valves are numbered 1-8, corresponding to the 8 diagonal areas connecting the 4 legs. The odd-numbered electric valves are filled with air pressure into the 1 and 3 areas of each leg. When the pressure is high, the legs are a backward 'S' shape; The even-numbered air circuit inflates the 2 and 4 areas of each leg, and the legs make a forward 'S' shape at high pressure.

When the soft quadruped robot is walking, an important index to measure its motion performance is the walking speed v, and the stride S and the delay time t jointly determine the walking speed v. When the air pressure is less than the deformation limit of 35 kPa, the greater the air pressure, the greater the stride. In order to increase the ventilation speed and reduce the fatigue of the leg structure under high deformation under high air pressure, based on the experimental test results of the foot end work space, taking into account the leg height and stride length, we choose the best model for the soft quadruped robot. The combination of air pressure is 30 kPa and 15 kPa (height $H = 225$ mm, stride S = 55 mm, maximum leg height is 95 mm) to test the speed and stability of the two gaits of the quadruped robot.

The legs of the soft quadruped robot designed in this paper are composed of drivers and soft materials, which are flexible structures, and their walking speed is greatly affected by the delay time t. The delay time t refers to the time from when the program sends instructions to controlling the air pressure drive to make the robot complete the desired motion and stabilize, including the adjustment time of the electric proportional valve, the time for inflating or deflation of the internal air pressure of the driver, and the time for stabilizing the structural deformation of the driving robot. Obviously, the smaller the delay time t, the faster the robot walks. However, it takes a certain amount of time for the legs to deform due to the expansion and shrinkage of the robot driver and the obvious hysteresis characteristics of the leg structure deformation. Therefore, when the delay time t is too short, the inflation and deflation speed of the air pressure

in the driver cannot keep up with the speed of the program signal, resulting in little or no deformation of the legs of the robot, resulting in disordered gait control and inability to move normally. In addition, in the process of walking, it can be observed that the deformation speed of the legs changes from slow to fast, and then slow again. The reason is that the deformation response of the leg structure is not sensitive when the air pressure is low or when the deformation is about to reach the limit value.

In order to explore the relationship between the delay time t and the movement speed of the soft robot, we measured the effect of the delay time t on the robot's walking speed v, and found that when the delay time t is less than 2 seconds, the response speed of the robot's legs cannot keep up. The speed of the program signal makes the quadruped robot unable to walk normally, which indicates that it takes at least 2 seconds for the robot legs to deform and maintain stability in order to achieve normal movement. Figure 26 shows a gait cycle in the straight-line walking process of the soft quadruped robot, which takes 12 seconds in total. In a gait cycle, the quadruped robot completes a displacement with a stride of, that is, the walking speed of the robot is v = 4.58 mm/s. Cycle the gait in the figure, and the robot can achieve continuous straight-line walking motion.

In addition, during the movement of the quadruped robot, the NI myRio platform is fixed to the position of the body (as shown by the black square platform in Figure 27) to test the stability of the robot during walking. Its sensor feedback information is shown in Figure 28. It can be seen that during the movement of the quadruped robot, the flip angles of the three coordinate axes do not exceed 15°, and there is no sudden change in angle, which proves that the robot has good stability when walking in a straight line.

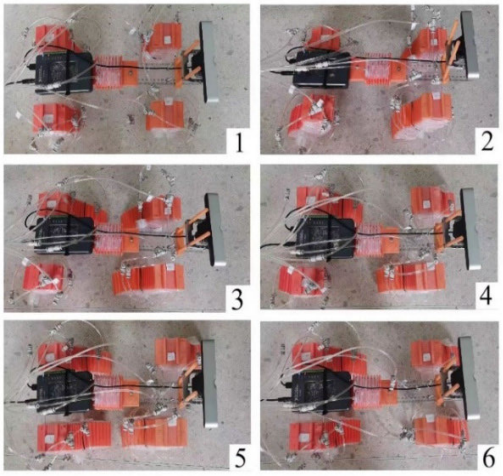

FIGURE 27. Straight walking experiment (Walk gait).

2) CURVE WALKING EXPERIMENT

The functions of the soft robot designed in this paper include curved walking, and the torsion structure of its waist controls the rotation angle of the robot head. Since the torsion structure contains two rows of drivers, if only one side is filled with air pressure to drive the rotation, the other side may have no air support, and its rotation angle cannot be controlled. Therefore, the method of differential pressure charging is adopted, and the rotation angle is controlled by using the different pressure difference between the left and the right. Firstly, it is necessary to conduct experimental measurements on the rotation angles caused by different degrees of pressure difference, and the experimental results are shown in Figure 29. It can be seen from the curve that within an appropriate pressure range, the greater the pressure difference, the greater the rotation angle, but an excessive pressure difference will cause the rotation angle to be too large, which is difficult to control and easily causes structural damage.

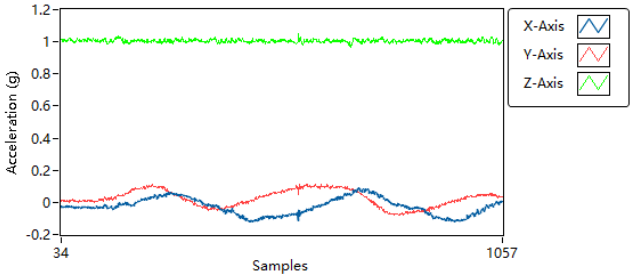

FIGURE 28. Yaw angular acceleration information.

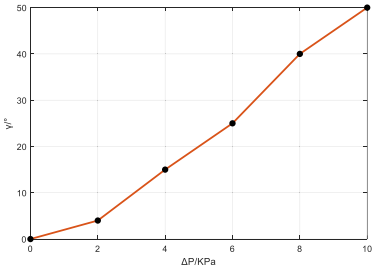

FIGURE 29. Relationship between differential pressure and rotation angle.

During the curved walking process of the soft quadruped robot, the air pressure difference of the drive in the waist is selected to be 0.4, that is, the torsion angle $y = 15°$. The experimental process is shown in Figure 30. The figure shows the first gait cycle. The first three steps are consistent with a straight-line walking gait. The fourth step is to add the rotation angle while stepping the left front leg to make the front half of the body rotate. After that, adjust the center of gravity according to right rear → right front → center of gravity → The gait sequence of left rear → left front performs cyclical movement; its air circuit sequence is also similar to that of the straight walking experiment, the difference is that in the fourth step of rotation, two electric valves need to be added to provide two different air pressures, so that the front end of the robot can Turning, so as to realize turning and walking in a curved line, verifies the steering ability of the soft quadruped robot. The deflection angle information collected by NI myRio during walking is shown in Figure 31. The

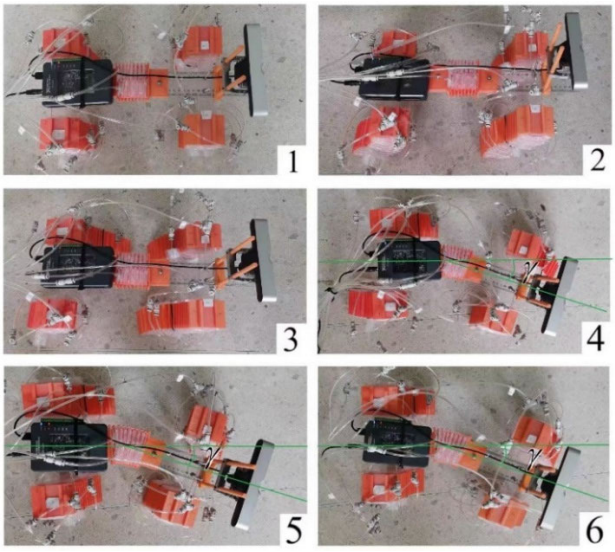

FIGURE 30. Relationship between air pressure and deformation in the diagonal area of a single leg.

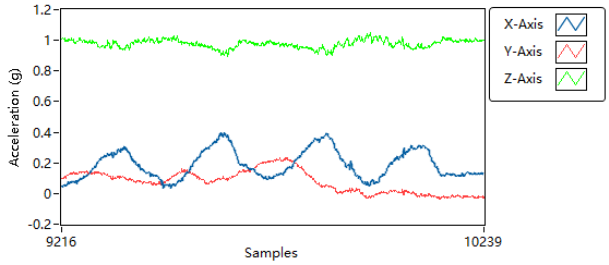

FIGURE 31. Yaw angular acceleration information.

deflection angles of the three coordinate axes do not exceed 20°, and there is no sudden change in angle, which proves that the robot has good stability during curved walking.

VI. CONCLUSION

In this paper, the motion mechanism and structure of quadrupeds and mollusks are analyzed, combined with relevant knowledge of bionics, materials science, and structural design; therefore, the motion and control of existing quadruped robots are improved and designed, and a bionic soft body quadruped robot is proposed. The research content involves the design and optimization of the robot's leg structure and driver, overall kinematics modeling, gait planning, simulation analysis of single-leg driving motion, and the design, construction and experimental verification of the control system. According to the structural design requirements, the robot prototype was actually produced, and a control system for adjusting multi-channel air pressure and gait was developed and built. A large number of simulations and experimental analyses were performed on the legs and the overall movement, and then verified by experiments. The various performance indexes of the soft quadruped robot prove the rationality and feasibility of the research design in this paper.

The specific research content of this paper is as follows:

(1) Aiming at the motion mechanism of the bionic soft quadruped robot, based on the deformation idea of the hexagonal honeycomb cavity structure, combined with the flexibility of mollusks, the robot leg structure is designed: including the external frame structure and internal pneumatic drive. The former is composed of two rows of hexagonal chamber structures, which are driven by the inflation and expansion of the latter for deformation, such as stretching, bending, and stepping; secondly, the parameters of the structure are analyzed and determined by finite element design; In addition, this structure is used to design the waist part of the robot, which is used to realize the turning function of the quadruped robot, and a horizontal holding structure is added to increase the stability of the quadruped robot. Based on the above structure, a bionic soft quadruped robot is developed and tested. Its production technology and method are designed in detail.

(2) Analyze the deformation principle of the hexagonal chamber and the elongation of the single leg by using the geometric method, and combine the method of segmental curvature to mathematically model the bending angle and bending radius of the single leg. The validity of the mathematical model is verified by finite element analysis of the length, bending angle and bending radius.

(3) A multi-channel air pressure control system is designed for the soft quadruped robot, including hardware selection and software design. Using this system to test the performance of soft mechanical legs, the specific results are as follows: within the experimental air pressure range (0-40 kPa), the elongation and bending angle have a similar trend, and when the air pressure is 35 kPa, they reach the maximum value, respectively 130 mm and 139°, combined with the static model in the third chapter and the simulation results, it is basically consistent; in the foot work space experiment, the relationship between the regional air pressure combination and the leg height and stride change is obtained; in the single leg experiment process, obvious hysteresis can be observed, that is, it takes a long time from the program instruction to the leg to complete the corresponding deformation motion and stabilize, the shortest is 2 s; in the walking experiment of the quadruped robot, according to the gait Plan the air sequence design, use the control system to realize the robot's straight line, curve turning and walking motion, and use NI myRio to record the deflection angle information during the whole process of motion, so as to verify the stability and motion ability of the two walking modes of the soft quadruped robot.

ACKNOWLEDGMENT

The authors would like to thank the Shanxi Scholarship Council of China for their support under the project "Soft Bionic Quadruped Robot Based on Honeycomb Structure" (Project No.: 2022-006).

REFERENCES

[1] D. Rus and M. T. Tolley, "Design, fabrication and control of soft robots," *Nature*, vol. 521, no. 7553, pp. 467–475, May 2015, doi: 10.1038/nature14543.

[2] M. T. Tolley, R. F. Shepherd, B. Mosadegh, K. C. Galloway, M. Wehner, M. Karpelson, R. J. Wood, and G. M. Whitesides, "A resilient, untethered soft robot," *Soft Robot.*, vol. 1, no. 3, pp. 213–223, Sep. 2014, doi: 10.1089/soro.2014.0008.

[3] R. K. Katzschmann, A. D. Marchese, and D. Rus, "Autonomous object manipulation using a soft planar grasping manipulator," *Soft Robot.*, vol. 2, no. 4, pp. 155–164, Dec. 2015, doi: 10.1089/soro.2015.0013.

[4] M. Cianchetti, C. Laschi, A. Menciassi, and P. Dario, "Biomedical applications of soft robotics," *Nature Rev. Mater.*, vol. 3, no. 6, pp. 143–153, May 2018, doi: 10.1038/s41578-018-0022-y.

[5] N. Ebrahimi, C. Bi, D. J. Cappelleri, G. Ciuti, A. T. Conn, D. Faivre, N. Habibi, A. Hošovský, V. Iacovacci, I. S. M. Khalil, V. Magdanz, S. Misra, C. Pawashe, R. Rashidifar, P. E. D. Soto-Rodriguez, Z. Fekete, and A. Jafari, "Magnetic actuation methods in bio/soft robotics," *Adv. Funct. Mater.*, vol. 31, no. 11, Mar. 2021, Art. no. 2005137, doi: 10.1002/adfm.202005137.

[6] E. T. Roche, M. A. Horvath, I. Wamala, A. Alazmani, S.-E. Song, W. Whyte, Z. Machaidze, C. J. Payne, J. C. Weaver, G. Fishbein, J. Kuebler, N. V. Vasilyev, D. J. Mooney, F. A. Pigula, and C. J. Walsh, "Soft robotic sleeve supports heart function," *Sci. Transl. Med.*, vol. 9, no. 373, Jan. 2017, Art. no. eaaf3925, doi: 10.1126/scitranslmed.aaf3925.

[7] L. Ohlmann and H. Mohammadi, "Soft robotic in the construction of prosthetic heart valve: A novel approach," *J. Med. Eng. Technol.*, vol. 44, no. 2, pp. 76–81, Feb. 2020, doi: 10.1080/03091902.2020.1723728.

[8] Y. Nishikawa and M. Matsumoto, "A design of fully soft robot actuated by gas–liquid phase change," *Adv. Robot.*, vol. 33, no. 12, pp. 567–575, Jun. 2019, doi: 10.1080/01691864.2019.1626281.

[9] W. Huang, J. Xiao, and Z. Xu, "A variable structure pneumatic soft robot," *Sci. Rep.*, vol. 10, no. 1, p. 18778, Nov. 2020, doi: 10.1038/s41598-020-75346-5.

[10] H. Liu, Z. Zhang, X. Zhu, and K. Xu, "A single-actuator gripper with a working mode switching mechanism for grasping and rolling manipulation," in *Proc. IEEE/ASME Int. Conf. Adv. Intell. Mechatronics (AIM)*, Jul. 2018, pp. 359–364, doi: 10.1109/AIM.2018.8452711.

[11] Y. Li, T. Ren, Y. Li, Q. Liu, and Y. Chen, "Untethered-bioinspired quadrupedal robot based on double-chamber pre-charged pneumatic soft actuators with highly flexible trunk," *Soft Robot.*, vol. 8, no. 1, pp. 97–108, Feb. 2021, doi: 10.1089/soro.2019.0137.

[12] M. Wehner, R. L. Truby, D. J. Fitzgerald, B. Mosadegh, G. M. Whitesides, J. A. Lewis, and R. J. Wood, "An integrated design and fabrication strategy for entirely soft, autonomous robots," *Nature*, vol. 536, no. 7617, pp. 451–455, Aug. 2016, doi: 10.1038/nature19100.

[13] Y. Hao, Z. Gong, Z. Xie, S. Guan, X. Yang, Z. Ren, T. Wang, and L. Wen, "Universal soft pneumatic robotic gripper with variable effective length," in *Proc. 35th Chin. Control Conf. (CCC)*, Jul. 2016, pp. 6109–6114, doi: 10.1109/ChiCC.2016.7554316.

[14] M. Ishida, D. Drotman, B. Shih, M. Hermes, M. Luhar, and M. T. Tolley, "Morphing structure for changing hydrodynamic characteristics of a soft underwater walking robot," *IEEE Robot. Autom. Lett.*, vol. 4, no. 4, pp. 4163–4169, Oct. 2019, doi: 10.1109/LRA.2019.2931263.

[15] M. Cianchetti, M. Calisti, L. Margheri, M. Kuba, and C. Laschi, "Bioinspired locomotion and grasping in water: The soft eight-arm OCTOPUS robot," *Bioinspiration Biomimetics*, vol. 10, no. 3, May 2015, Art. no. 035003, doi: 10.1088/1748-3190/10/3/035003.

[16] S. Seok, C. D. Onal, K.-J. Cho, R. J. Wood, D. Rus, and S. Kim, "Meshworm: A peristaltic soft robot with antagonistic nickel titanium coil actuators," *IEEE/ASME Trans. Mechatronics*, vol. 18, no. 5, pp. 1485–1497, Oct. 2013, doi: 10.1109/TMECH.2012.2204070.

[17] Y. She, C. Li, J. Cleary, and H.-J. Su, "Design and fabrication of a soft robotic hand with embedded actuators and sensors," *J. Mech. Robot.*, vol. 7, no. 2, pp. 021007-1–021007-9, May 2015, doi: 10.1115/1.4029497.

[18] C. Xiong and Y. Xiong, "Stability index and contact configuration planning for multifingered grasp," *J. Robotic Syst.*, vol. 15, no. 4, pp. 183–190, 1998, doi: 10.1002/(SICI)1097-4563(199804)15:4<183:AID-ROB1>3.0.CO;2-L.

[19] N. Jinqiang, T. Chaoyang, and L. Yuxiang, "Inchworm inspired pneumatic soft robot based on friction hysteresis," *J. Robot. Autom.*, vol. 1, no. 2, Sep. 2017, Art. no. 1.

[20] J. Najem, S. A. Sarles, B. Akle, and D. J. Leo, "Biomimetic jellyfish-inspired underwater vehicle actuated by ionic polymer metal composite actuators," *Smart Mater. Struct.*, vol. 21, no. 9, Aug. 2012, Art. no. 094026, doi: 10.1088/0964-1726/21/9/094026.

[21] E. Coevoet, A. Escande, and C. Duriez, "Optimization-based inverse model of soft robots with contact handling," *IEEE Robot. Autom. Lett.*, vol. 2, no. 3, pp. 1413–1419, Jul. 2017, doi: 10.1109/LRA.2017.2669367.

[22] H. Jiang, Z. Wang, Y. Jin, X. Chen, P. Li, Y. Gan, S. Lin, and X. Chen, "Hierarchical control of soft manipulators towards unstructured interactions," *Int. J. Robot. Res.*, vol. 40, no. 1, pp. 411–434, Jan. 2021, doi: 10.1177/0278364920979367.

[23] C. Li, Y. Xie, X. Huang, J. Liu, Y. Jin, and T. Li, "Novel dielectric elastomer structure of soft robot," *Proc. SPIE*, vol. 9430, pp. 468–473, Apr. 2015, doi: 10.1117/12.2084015.

[24] *Structure and Gait Optimization of a Soft Quadrupedal Robot*. Accessed: Jun. 23, 2024. [Online]. Available: https://so1.typicalgame.com/scholar?hl=en&as_sdt=0%2C47&q=Structure+and+Gait+Optimization+of+a+Soft+Quadrupedal+Robot&btnG=

[25] Z. Jiang, Y. Wang, and K. Zhang, "Development of a pneumatically actuated quadruped robot using soft–rigid hybrid rotary joints," *Robotics*, vol. 13, no. 2, p. 24, Jan. 2024, doi: 10.3390/robotics13020024.

[26] H. Mei, Z. Han, S. Liang, and F. K. Ko, "Process modelling of 3D hexagonal braids," *Compos. Struct.*, vol. 252, Nov. 2020, Art. no. 112679, doi: 10.1016/j.compstruct.2020.112679.

MENG HONGJUN received the B.S. and M.S. degrees in mechanical and electronic engineering from Zhejiang University of Technology, in 2003 and 2010, respectively, the Ph.D. degree in mechanical and electronic engineering from Beihang University, in 2015, and the Ph.D. degree in mechanical and electronic engineering from Taiyuan University of Technology, in 2017. From 2017 to 2019, he was a Lecturer with the School of Mechanical Automation and Software, Shanxi University, where, he has been an Associate Professor, since 2019. His research interests include biomedical engineering and robot control.

ZHANG SHUPENG is currently pursuing the master's degree with the School of Automation and Software, Shanxi University, China. His research interest includes soft robot design and control.

ZHANG WEI is currently pursuing the master's degree with the School of Automation and Software, Shanxi University. His research interest includes design and control of soft robots.

REN YUKE is currently pursuing the degree in control engineering with the School of Automation and Software, Shanxi University. Her research interests include soft robotics and robot control.